

# Ideal MHD induced temperature flattening in spherical tokamaks

Cite as: Phys. Plasmas **30**, 042507 (2023); <https://doi.org/10.1063/5.0141858>

Submitted: 09 January 2023 • Accepted: 12 March 2023 • Published Online: 04 April 2023

 S. C. Jardin,  N. M. Ferraro,  W. Guttenfelder, et al.



View Online



Export Citation



CrossMark



**Physics of Plasmas**  
Features in Plasma Physics Webinars

Register Today!



# Ideal MHD induced temperature flattening in spherical tokamaks

Cite as: Phys. Plasmas **30**, 042507 (2023); doi: 10.1063/5.0141858

Submitted: 9 January 2023 · Accepted: 12 March 2023 ·

Published Online: 4 April 2023



View Online



Export Citation



CrossMark

S. C. Jardin,<sup>a)</sup> N. M. Ferraro, W. Guttenfelder, S. M. Kaye, and S. Munaretto

## AFFILIATIONS

Princeton Plasma Physics Laboratory, P. O. Box 451, Princeton, New Jersey 08543, USA

**Note:** This paper is part of the Special Collection: Papers from the 64th Annual Meeting of the APS Division of Plasma Physics.

**Note:** Paper PII 2, Bull. Am. Phys. Soc. **67** (2022).

<sup>a)</sup>Invited speaker. Author to whom correspondence should be addressed: [jardin@pppl.gov](mailto:jardin@pppl.gov)

## ABSTRACT

This paper extends the analysis first presented in Jardin *et al.* [Phys. Rev. Lett. **128**, 245001 (2022)] to more thoroughly examine the stability of spherical torus equilibrium to ideal magnetohydrodynamic (MHD) infernal modes and their nonlinear consequences. We demonstrate that in a 3D resistive magnetohydrodynamic (MHD) simulation of a NSTX discharge, anomalous transport can occur due to these instabilities. We generate a family of equilibrium of differing  $\beta$  and use this to show that these instabilities could explain the experimentally observed flattening of the electron temperature profile at modest  $\beta$ . The modes studied in this paper are found to occur with poloidal mode number  $m$  and toroidal mode number  $n$  when the ratio  $m/n$  is in the range of 1.2–1.5, when the central safety factor is in this range or slightly lower, and when the central region has very low magnetic shear. Our analysis gives some insight as to why the unstable linear growth rates are oscillatory functions of the toroidal mode number  $n$ . We present a simulation of an initially stable configuration that passes through a stability boundary at a critical  $\beta$  as it is heated. We also show that a particular NSTX discharge is unstable to these modes over a timescale of several hundred ms. We conclude that these modes must be taken into account when performing predictive modeling. An appendix shows that similar modes can be found in  $R/a = 4$  tokamaks for certain q-profiles and  $\beta$  values.

Published under an exclusive license by AIP Publishing. <https://doi.org/10.1063/5.0141858>

## I. INTRODUCTION

A recent paper<sup>1</sup> suggests that ideal magnetohydrodynamic (MHD) instabilities may play a role in enhancing the effective electron thermal conductivity in high- $\beta$  discharges in NSTX<sup>2</sup> and other spherical tokamaks. These global pressure-driven instabilities, known as infernal modes,<sup>3</sup> are localized around low order rational surfaces and linearly exhibit distinct toroidal mode structure,  $n$ , and poloidal mode structure  $m$ . They tend to be radially localized in low-magnetic shear regions near the center of the discharge with  $m/n \geq q_0$ , where  $q_0$  is the central safety factor. Although the modes have radially localized linear eigenfunctions, their nonlinear evolution can destroy magnetic surfaces near the center of the discharge and thus severely degrade magnetic confinement there.

The onset of these pressure-driven ideal MHD modes and the associated surface breakup in the central region could explain why global energy confinement times for boronized wall, H-mode plasmas in the NSTX spherical tokamak were observed to have a near-linear  $B_T$ -scaling, stronger than typically observed in conventional aspect

ratio tokamaks.<sup>4,5</sup> This  $B_T$  scaling is also observed in other STs, such as MAST<sup>6</sup> and Globus-M and -M2.<sup>7,8</sup>

It has also been observed in NSTX that for moderate to high- $\beta$  discharges, the electron temperature profiles tend to be broadened, i.e., gradients in the outer radius steepen, while  $T_e$  at the magnetic axis remains largely unchanged as  $\beta$  increases.<sup>4,9,10</sup> The present consensus is that this core  $T_e$ -flattening and change in  $\chi_e$  cannot be explained simply by  $\nabla T_e$ -driven drift wave mechanisms.

We note here that multiple other hypotheses have been put forth for explaining this behavior, including high frequency global and compressional Alfvén eigenmodes (GAE/CAE)<sup>10–13</sup> and the coupling of CAE modes to kinetic Alfvén waves (KAW).<sup>14</sup> However, the estimated magnitude of transport and/or energy coupling from these mechanisms are not typically large enough to entirely explain the NSTX observations.<sup>15</sup>

In this paper, we advance the hypothesis first presented in Ref. 1 that low- $n$ , core, pressure-driven ideal MHD instabilities that are non-disruptive can breakup flux surfaces, ultimately leading to enhanced

stochastic transport that preferentially influences electron thermal losses. This surface breakup is significant since the micro-turbulence codes assume that good magnetic flux surfaces exist, which should be the case in the absence of MHD instabilities and magnetic islands. The partial destruction of the surfaces in the core region leads to another transport mechanism and possibly explains the observed electron temperature flattening and strong  $B_T$  dependence of  $\tau_E$  in STs.

This surface breakup, observed in the 3D MHD simulations, is consistent with the recent work by Boozer,<sup>16</sup> which shows that ideal MHD instabilities can lead to magnetic surface breakup, even for an arbitrary small resistivity. If the magnetic surfaces are destroyed in the vicinity of large pressure gradients, anomalous transport will occur by way of parallel diffusion, which is much greater than diffusion across flux surfaces. We have investigated this mechanism by applying the 3D resistive MHD code M3D-C1<sup>17</sup> to some reconstructed NSTX equilibrium.

The remainder of this paper is organized as follows: Sec. II presents a brief review of internal pressure-driven ideal MHD instabilities in tokamaks. In Sec. III, we discuss the linear and non-linear analysis of one particular equilibrium for NSTX shot 124 379 in detail. In Sec. IV, we use a scaling technique to generate a family of equilibrium with differing  $\beta$  from that one equilibrium. In Sec. V, we present the results of a nonlinear calculation in which we start with a low- $\beta$  stable equilibrium and apply heating power to increase  $\beta$  and thus drive it through a stability boundary. In Sec. VI, we return to NSTX shot 124 379 and show the results of stability analysis every 10 ms for 200 ms in the discharge. We present a summary and some conclusions in Sec. VII. In the Appendix, we present some stability results for a model circular  $R/a = 4$  equilibrium that extends some analysis presented in Ref. 3.

## II. PRESSURE-DRIVEN IDEAL MHD INSTABILITIES

It is well known that a tokamak equilibrium is unstable to internal ideal MHD instabilities if there is a displacement field  $\xi(\mathbf{x})$  that makes the energy functional  $\delta W_f$  negative.<sup>18</sup> A particular form of this functional provides physical insight as it shows that  $\delta W_f$  can be written as an integral with five terms, three of which are positive definite.<sup>19,20</sup> The remaining two terms, which can be negative, involve the pressure gradient and the parallel current, respectively. If the term involving the pressure gradient dominates, we call these pressure-driven modes.

There are three classes of internal pressure-driven instabilities in tokamaks that have been identified: interchange modes, ballooning modes, and infernal modes. Stability to interchange modes can be evaluated by a criterion developed by Mercier<sup>21</sup> involving an expansion around the magnetic axis. In simplified geometry, this criterion predicts stability if the central safety factor is greater than unity,  $q_0 > 1$ , and there is non-zero magnetic shear.

Ballooning modes<sup>22,23</sup> occur in regions of high magnetic shear. They are azimuthally localized in the low field region. The modes with the highest toroidal mode number  $n$  are the most unstable. These modes do not require a rational surface. In the high- $n$  limit, each magnetic surface can be examined separately by solving a 1D ordinary differential equation.

In contrast, infernal modes<sup>3</sup> occur in regions of low magnetic shear. They are not azimuthally localized, but have a distinct poloidal mode number  $m$ . Modes with intermediate toroidal mode number,

$n \geq 2$ , are typically the most unstable. These modes are global, but radially localized around a rational surface. They can be unstable at significantly lower values of  $\beta$  than ballooning modes. These modes require global analysis, for example, by codes such as PEST,<sup>24</sup> GATO,<sup>25</sup> or M3D-C1.<sup>17</sup> The growth rates are normally oscillatory functions of the toroidal mode number  $n$ . These modes are not as well known as ballooning modes. One reason for this is that they were identified just as the classic book on Ideal MHD by Freidberg<sup>26</sup> was coming out and are not mentioned in that book. This paper is about the effect of these instabilities in NSTX and other STs and tokamaks.

## III. A TYPICAL CASE

Consider the equilibrium from NSTX shot 124 379 at time 640 ms shown in Fig. 1 of Ref. 1. This has  $RB_T = 0.418$  m-T, plasma current  $I_p = 990$  kA,  $\beta = 6.8\%$ ,  $\beta_N = \beta_T(\%) \times B_T(T) \times a(m)/I_p(\text{MA}) = 3.9$ , and central safety factor  $q(0) = 1.29$ . Some experimental details of the discharge and this time slice are given in Ref. 27. Our analysis shows that this equilibrium is unstable to many low- $n$  (toroidal mode number) ideal MHD modes as shown in Figs. 1 and 2.

We see from Fig. 2 that each unstable toroidal mode with mode number  $n$  has a linear eigenfunction with a distinct poloidal mode number  $m$ . We list in Table I the poloidal mode numbers associated with the first 15 unstable toroidal modes shown in Fig. 1. These are seen to be such that the ratio  $m/n$  is in the range of  $1.33 \leq m/n \leq 1.42$ . We see from Fig. 3 that these rational numbers align with a  $q$  value just above  $q_0$  and in the low-shear part of the discharge.

As explained in Sec. II, pressure-driven, radially localized, ideal MHD modes, such as these, which occur in low shear regions at pressure-gradient values below the ideal MHD infinite- $n$  ballooning limit,<sup>22</sup> and where the growth rate is an oscillatory function of the toroidal mode number  $n$ , have been referred to as infernal modes.<sup>3,28–30</sup>

Table I and Fig. 3 give us some insight as to why the modes with  $n = 2$  and  $n = 4$  are stable for this equilibrium. For  $n = 2$ , modes with  $m \leq 2$  are not resonant, and modes with  $m \geq 3$  are outside the low

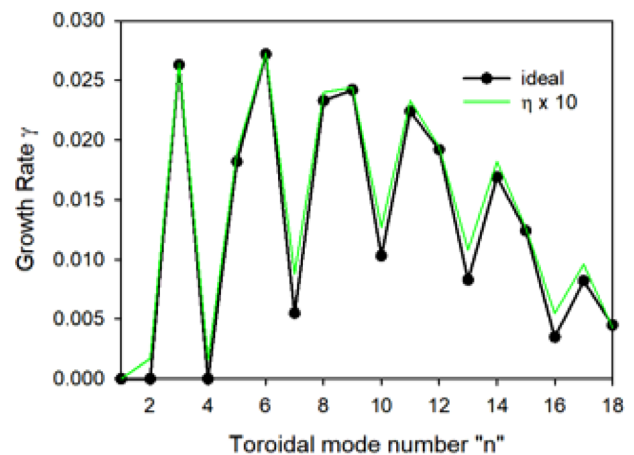
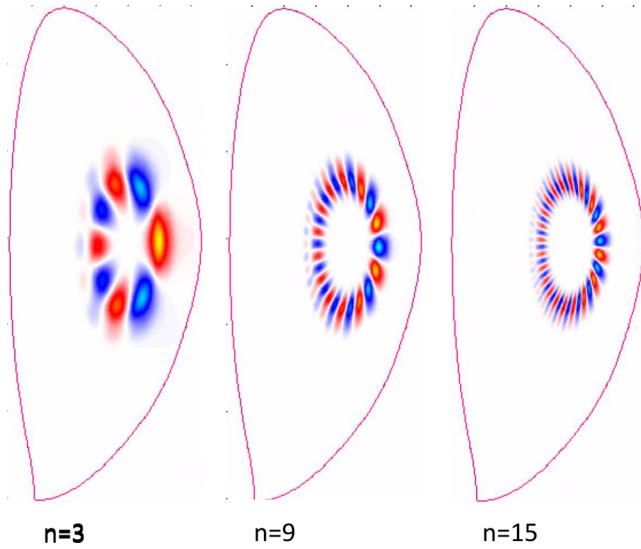


FIG. 1. Normalized growth rates for unstable modes with toroidal mode numbers 1–18 for NSTX shot 124 379 @640 ms using temperature-dependent Spitzer resistivity. Also shown (in green online) are the growth rates with the resistivity increased by 10, indicating that these are ideal MHD instabilities. Reproduced with permission from Jardin *et al.*, Phys. Rev. Lett. **128**, 245001 (2022). Copyright 2022 American Physical Society.



**FIG. 2.** Linear eigenmodes showing pressure contours for modes with  $n=3$ , 9, and 15 from Fig. 1. Other modes have similar structure, with poloidal mode number  $m \sim (4/3)n$ . Reproduced with permission from Jardin *et al.*, Phys. Rev. Lett. **128**, 245001 (2022). Copyright 2022 American Physical Society.<sup>1</sup>

**TABLE I.** Poloidal mode number  $m$  for each of first 15 unstable modes shown in Fig. 1.

$n$	3	5	6	7	8	9	10	11	12	13	14	15	16	17	18
$m$	4	7	8	10	11	12	14	15	16	18	19	20	22	23	24

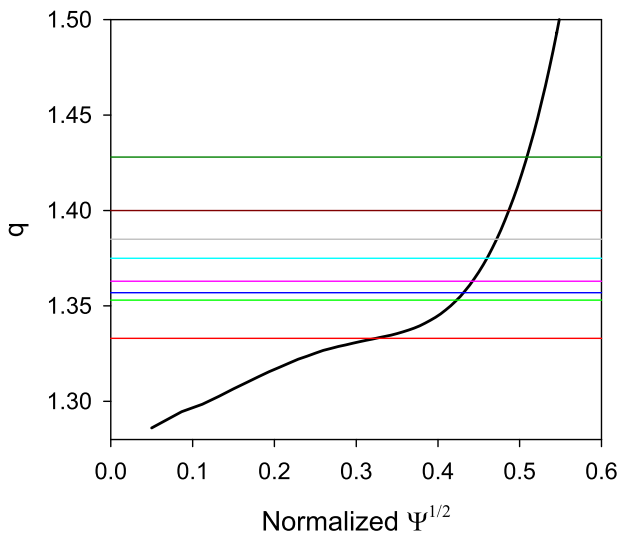


**FIG. 3.** Close-up of the central portion of the  $q$ -profile for NSTX shot 124379 time 640 ms plotted against the square root of the normalized poloidal flux. The  $m/n$  values from Table I are shown as horizontal lines.

shear region. Similarly, for  $n=4$ , modes with  $m \leq 5$  are not resonant, and those with  $m \geq 6$  are outside the low shear region.

Because this equilibrium is unstable to ideal MHD modes, it is unlikely that this equilibrium file is a true representation of the experimental equilibrium at that time. Nevertheless, we evolve this configuration in time to see if it evolves into a nearby stable equilibrium state.

For simplicity, we used the single-fluid form of the 3D nonlinear M3D-C1 code to advance the particle density  $n$ , the fluid velocity  $\mathbf{V}$ , the plasma pressure  $p$ , and the magnetic scalar and vector potentials  $\Phi$  and  $\mathbf{A}$  according to the following partial differential equations:

$$\frac{\partial n}{\partial t} + \nabla \cdot (n\mathbf{V}) = \nabla \cdot D\nabla n, \tag{1}$$

$$\frac{\partial \mathbf{A}}{\partial t} = -\mathbf{E} - \nabla\Phi, \tag{2}$$

$$\nabla_{\perp} \cdot \frac{1}{R^2} \nabla\Phi = -\nabla_{\perp} \cdot \frac{1}{R^2} \cdot \mathbf{E}, \tag{3}$$

$$\mathbf{E} + \mathbf{V} \times \mathbf{B} = \eta\mathbf{J}, \tag{4}$$

$$nM_i \left( \frac{\partial \mathbf{V}}{\partial t} + \mathbf{V} \cdot \nabla\mathbf{V} \right) + \nabla p = \mathbf{J} \times \mathbf{B} - \nabla \cdot \Pi, \tag{5}$$

$$\frac{3}{2} \left[ \frac{\partial p}{\partial t} + \nabla \cdot (p\mathbf{V}) \right] = -p\nabla \cdot \mathbf{V} + \mathbf{J} \cdot \mathbf{E} - \nabla \cdot \mathbf{q} + S_E. \tag{6}$$

The magnetic field and current density are then determined by  $\mathbf{B} = \nabla \times \mathbf{A}$  and  $\mathbf{J} = \nabla \times \mathbf{B}$ . The symbol  $\nabla_{\perp}$  in Eq. (3) refers to the gradient in the  $(R, Z)$  plane in a  $(R, \phi, Z)$  cylindrical coordinate system. Equation (3) follows from the gauge condition on  $\mathbf{A}$ ,  $\nabla_{\perp} \cdot R^{-2}\mathbf{A} = 0$ . The temperature is the pressure divided by the density,  $T \sim p/n$ . The linear form of the code used for linear stability studies is just the linearized form of these same equations.

The particle diffusion term  $D$  in Eq. (1) is a small term included to aid numerical stability. The resistivity  $\eta$  in Eq. (4) is the temperature-dependent Spitzer function<sup>31</sup> with no enhancement. The stress tensor in Eq. (5) is of standard form for viscosity,<sup>32</sup> with viscosity coefficient  $\mu$ . The heat flux vector,  $\mathbf{q}$ , in Eq. (6) has both an isotropic part and a part parallel to the magnetic field:  $\mathbf{q} = -\kappa\nabla T - \kappa_{\parallel} \mathbf{b}\mathbf{b} \cdot \nabla T$ , where  $\mathbf{b}$  is a unit vector in the direction of the magnetic field.

The M3D-C1 code uses finite elements in all three dimensions. In the  $(R, Z)$  plane, these are unstructured “Bell” triangular elements<sup>33</sup> that, for most of these calculations, vary in size from  $h = 4$  cm near the separatrix to 1 cm near the axis, with a total of 10346 elements per plane. In these calculations, we normally use 24 planes, with structured equally spaced Hermite cubic finite elements.

In Ref. 1, we describe some convergence tests where we redid some calculations on grids with 28 792 and 38 063 elements per plane and with 36 and 48 planes. These tests led to the conclusion that the calculation was adequately converged, although it was not a rigorous convergence test. Within each 3D toroidal prism element is a polynomial in  $(R, \phi, Z)$  with 72 coefficients. The numerical error should vary as  $h^5$  within a plane and  $h^4$  in the toroidal direction.

This evolution was for 6000 Alfvén times,  $\tau_A$ , corresponding to about 2.75 ms. We used very small dimensionless transport coefficients to avoid them changing the profiles significantly by themselves, and to avoid the need for a density and energy source. (Ohmic heating was present but was negligible for the resistivity and time scales involved.) The plasma current was maintained at the initial level by adjusting the

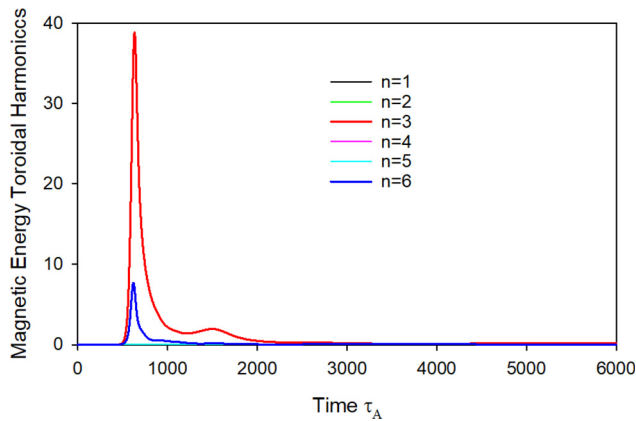


**FIG. 4.** Magnetic energy in the first six toroidal harmonics for the 6000  $\tau_A$  nonlinear simulation (AU).  $n = 0$  energy not shown.

loop voltage at the boundary. In code units, the dimensionless values were  $D = 10^{-6}$ ,  $\kappa = 10^{-6}$ , and  $\mu = 10^{-6}$  (to get the values in  $m^2/s$ , divide by  $\tau_A = 4.58 \times 10^{-7}s$ ). In contrast, the dimensionless parallel thermal conductivity was  $\kappa_{||} = 10$ , 7 orders of magnitude greater than  $\kappa$ . In code dimensionless units, the resistivity on axis corresponding to the Spitzer resistivity of a 916 eV plasma was initially  $\eta = 2 \times 10^{-8}$ .

The magnetic energy in the first six toroidal harmonics is shown in Fig. 4 for the nonlinear calculation up to  $t = 6000 \tau_A$ . Poincaré plots of the configuration at four times in the evolution can be found in Fig. 4 of Ref. 1.

The initial configuration was linearly unstable as we saw in Figs. 1 and 2. Nonlinearly, the  $n = 3$  mode grows largest, and around the time  $t = 500 \tau_A$  deforms the surfaces, primarily those near  $q = 4/3$  with a dominantly  $m = 4$  poloidal variation. The stochastic region near and interior to that surface causes the temperature and pressure to drop there, restabilizing the plasma. The detailed structure of the stochastic region rearranges itself, but at the final time,  $t = 6000 \tau_A$  the

configuration is again stable with only a small dominantly  $n = 3$  toroidal variation.

We show in Fig. 5(a) the midplane temperature profile for the initial state and the results at time  $t = 3200 \tau_A$  (1.46 ms) for the baseline calculation. We also show in Fig. 5(b) the results at the same time for a companion calculation that included sheared toroidal rotation (25 kH in the center) in the initial equilibrium. This rotation, which was present in the experiment, is seen to smooth the evolved temperature profile but not to qualitatively change the result.

It is seen that the temperature has decreased significantly in the center, near the magnetic axis, but has actually increased at mid-radius. Thus, the result of the ideal instabilities and associated parallel transport on the ergodic field lines was to effectively increase the transport in the center, near the original magnetic axis. This increase in the effective thermal conductivity in the center, over that which would be expected from microinstabilities alone, may explain similar experimental observations.<sup>10</sup>

#### IV. A FAMILY OF EQUILIBRIUM WITH DIFFERING $\beta$ VALUES

To further study and better quantify the effect of the ideal instabilities, we have generated a family of initial equilibrium states by applying Bateman scaling<sup>34</sup> to the initial equilibrium reconstruction. This scaling leaves the toroidal current density,  $Rp' + R^{-1}FF'$ , and hence the poloidal flux  $\Psi$ , unchanged but increases or decreases the toroidal field strength by a factor  $F_S$  at the separatrix. It does not require resolving the Grad-Shafranov equation, but only integrating the ordinary differential equation for  $F$  with a new boundary value,  $F_S$ . We generated two additional initial equilibrium states by setting this factor to be  $F_S = 0.9$  and  $F_S = 1.1$ . This generated additional initial equilibrium with  $(\beta = 8.2\%, q(0) = 1.2)$  and  $(\beta = 5.0\%, q(0) = 1.4)$ , respectively.

We redid the calculation with each of these initial equilibrium states and plot the midplane electron temperature at  $t = 1200 \tau_A$  for these and the original configuration in Fig. 6(b).

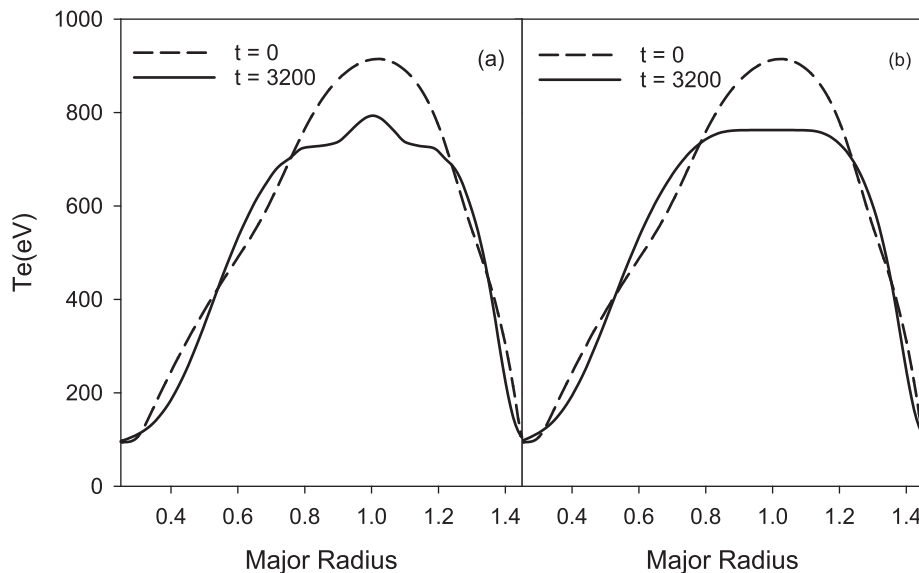


**FIG. 5.** Midplane temperature profiles for the initial state and for the results of the calculation at  $t = 3200 \tau_A$  (a) for the baseline calculation and (b) for a companion calculation in which sheared toroidal rotation was included with 25 kH in the center.

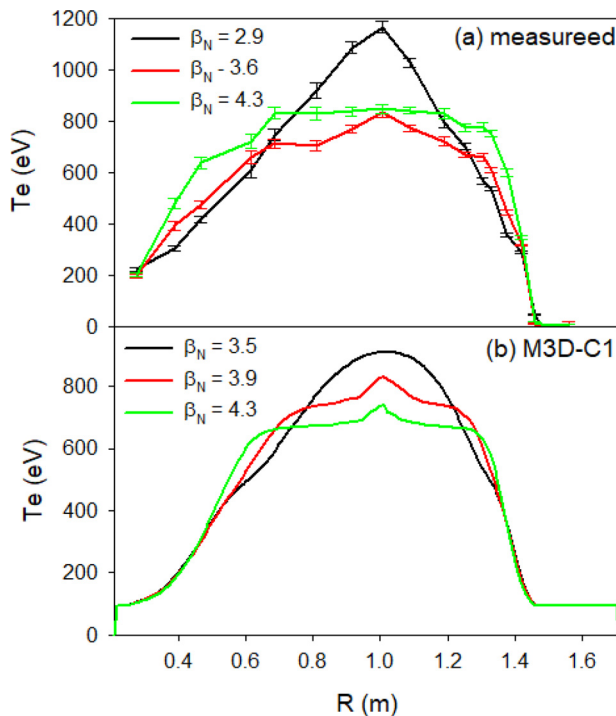


**FIG. 6.** (a) Experimental midplane electron temperature for the three equilibria considered in Refs. 10 and 35. (b) M3D-C1 midplane electron temperature at time  $t = 1200 \tau_A$  starting from the three Bateman scaled equilibria corresponding to  $F_S = 1.1$ ,  $F_S = 1.0$  (the original), and  $F_S = 0.9$ . Reproduced with permission from Jardin *et al.*, Phys. Rev. Lett. 128, 245001 (2022). Copyright 2022 American Physical Society.<sup>1</sup>

The profile labeled  $\beta_N = 3.5$  in Fig. 6(b) corresponds to an equilibrium configuration with  $F_S = 1.1$  that was MHD stable and so it retained good nested magnetic surfaces and the central temperature changed little from its initial value. The curve labeled  $\beta_N = 3.9$  was taken from the equilibrium used in Fig. 5, with  $F_S = 1.0$ . The destruction of the magnetic surfaces in the center led to a central flattening of the temperature profile. The curve labeled  $\beta_N = 4.3$  corresponds to an equilibrium with  $F_S = 0.9$  that was initially even more unstable than that of the original equilibrium and that increased instability led to a larger region in the center with destroyed surfaces and flattened temperature profile.

Each of the two unstable equilibria were linearly unstable to many modes, but the dominant nonlinear mode in the  $F_S = 0.9$  case was the (5, 4) (poloidal, toroidal) mode, whereas for the  $F_S = 1.0$  case, it was the (4, 3) mode. This shift was due to the change in the  $q$ -profile and associated rational surfaces due to the change in the toroidal field. In Fig. 7, we show the linear eigenfunctions of the two modes that become dominant non-linearly for the two equilibria.

In Fig. 6(a), we plot three experimentally measured midplane electron temperature profiles taken from the shots analyzed in Refs. 10 and 35. While not meant to be an exact comparison, we see the same qualitative behavior between the experimental profiles (a) and the simulation profiles in (b). At low enough  $\beta_N$ , the profiles are most peaked. As  $\beta_N$  increases, the profiles flatten near the axis, but steepen at

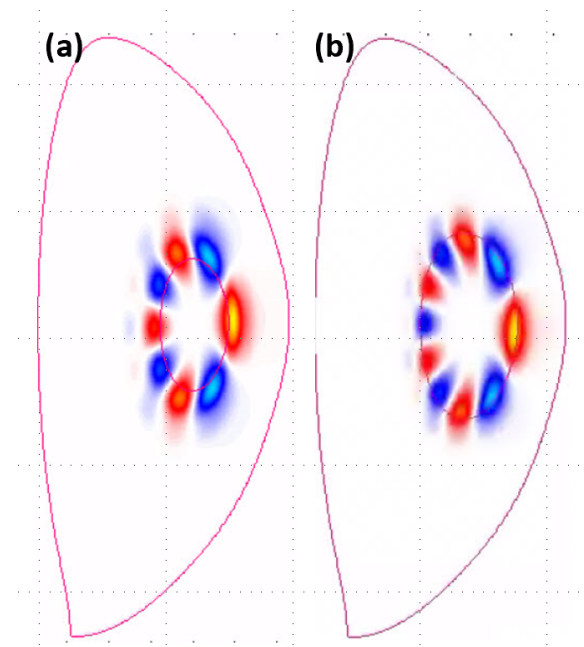


**FIG. 7.** (a) (4,3) mode located near the  $q = 1.33$  surface for the original equilibrium with  $F_S = 1.0$ . (b) (5,4) mode located near the  $q = 1.25$  surface for the Bateman scaled equilibrium with  $F_S = 0.9$ .

mid-radius. The simulations seem to have reproduced the most dominant experimental characteristic.

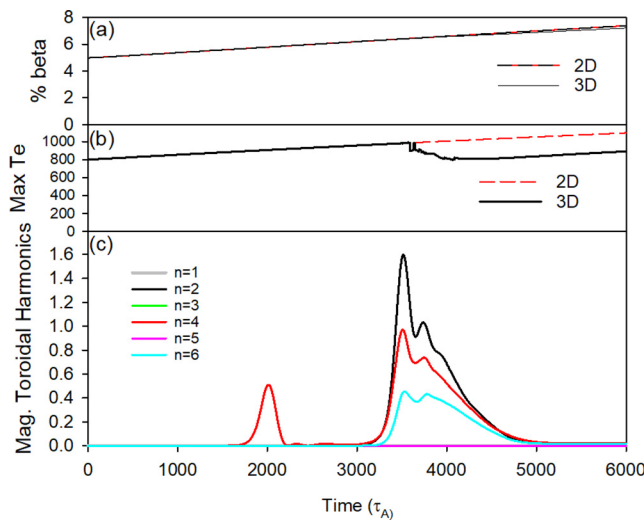
## V. APPLY HEATING TO A STABLE EQUILIBRIUM

The scan in Sec. IV was somewhat unphysical because the scaled equilibrium with  $F_S = 1.0$  and  $F_S = 0.9$  was unstable and so unlikely to have occurred in an experiment. In an attempt to make a more physical calculation, we begin with the stable equilibrium with  $F_S = 1.1$ , apply a heating source, and run for  $6000 \tau_A$ , or about 2.8 ms. The heating source had spatial dependence  $S_E \sim \exp(-((R - R_0)^2 + (Z - Z_0)^2)/\delta^2)$ , where  $R_0 = 1.0$  m,  $Z_0 = 0.0$ , and  $\delta = 0.4$  m. To shorten the calculation, we applied an unrealistically large heating source of 32 MW. The results are presented in Figs. 8–13.

We perform this calculation in both 2D (with no toroidal variation) and 3D to highlight the effect of the 3D instabilities by comparing the two. Figure 8(a) shows the plasma  $\beta$  as a function of time for both 2D and 3D calculations, the two curves essentially overlaying. Figure 8(b) shows the maximum electron temperature as a function of time. It is seen that the curves overlay until about  $t = 3500 \tau_A$ , at which time the temperature in the 2D calculation continues to increase, whereas it starts decreasing in the 3D calculation.

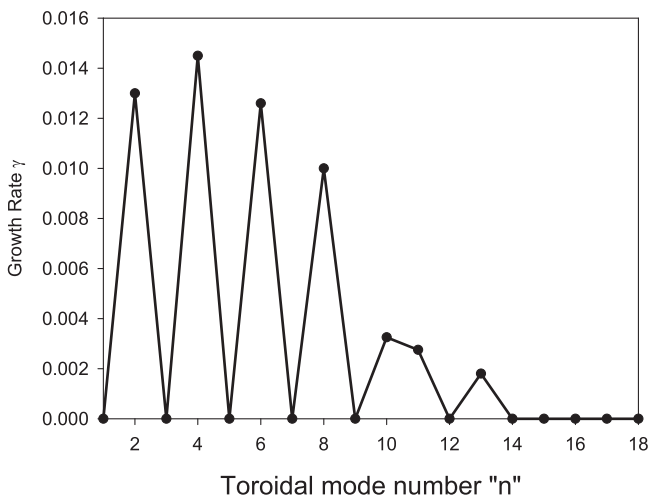
We paused the 2D calculation at  $t = 3000 \tau_A$ , just as the 3D calculation was starting to exhibit instabilities, to see which modes were linearly unstable. This is illustrated in Fig. 9 and Table II.

Table II shows that the linearly unstable modes at this time had rational values of  $m/n$  ranging from about 1.45 to 1.50. These unstable resonances are illustrated in Fig. 10 along with a blow-up of the  $q$ -profile near the origin. Comparing Figs. 3 and 10, we see that the Bateman scaling increased the value of  $q_0$  by about 10%, leading to a different set of rational surfaces lying in the low-shear region.



**FIG. 8.** (a) Percent  $\beta$  vs time for the 2D and 3D calculations. (b) Maximum electron temperature vs time for the 2D and 3D calculations. (c) Magnetic energy in the different toroidal harmonics for the 3D calculation as a function of time.

We can gain some understanding of why the growth rate shown in Fig. 9 is an oscillatory function of the toroidal mode number  $n$  by looking at the first few  $n$  values and where their resonances occur in Fig. 10. The first unstable mode,  $n = 2$ , has a resonance with  $m = 3$  at the edge of the low-shear region at  $q = 1.5$ . For the next few even  $n$ 's,  $n = 4, 6, 8, \dots$ , there is a  $m$  value that gives them a resonance at the same location. However, for the first few odd modes, there is no such resonance. For  $n = 3$ , modes with  $m \leq 4$  have no resonance, and modes with  $m \geq 5$  have their resonance outside the low shear regime. Similarly, for  $n = 5$ , modes with  $m \leq 7$  have no resonance, whereas those with  $m \geq 8$  have resonance outside the low shear regime. This



**FIG. 9.** Normalized growth rates for unstable modes with toroidal mode numbers 1–18 for initially stable 2D calculation with heating applied at time  $t = 3000 \tau_A$  using temperature-dependent Spitzer resistivity.

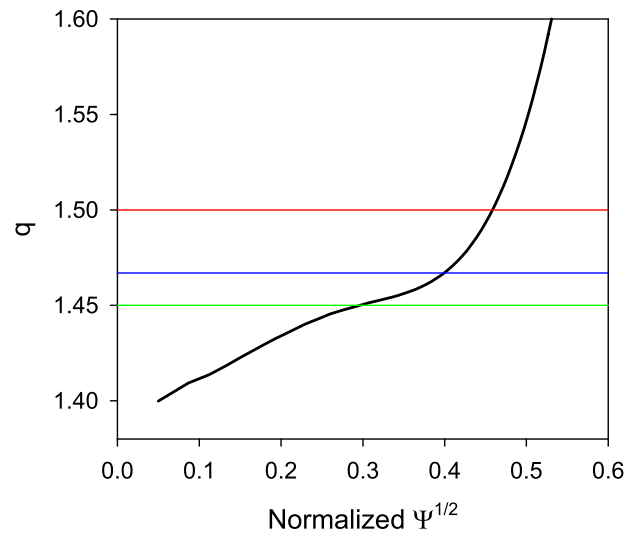


**FIG. 10.** Close-up of the central portion of the  $q$ -profile for Bateman scaled, initially stable, equilibrium plotted against the squareroot of the normalized poloidal flux. The  $m/n$  values from Table II are shown as horizontal lines.

difference in the possible resonant locations of the odd and even toroidal mode numbers give rise to the oscillation with  $n$  shown in Fig. 9.

Figure 8(c) shows the magnetic energy in the different toroidal harmonics in the 3D calculation as a function of time. There is a slight blip in the  $n = 4$  energy at  $t = 2000 \tau_A$ , which did not noticeably affect the peak electron temperature. However, at about  $t = 3500 \tau_A$ , a large  $n = 2$  disturbance grows up, saturates, and restabilizes. This  $n = 2$  mode is seen to nonlinearly drive  $n = 4$  and  $n = 6$  disturbances and is seen to coincide with the drop of the central electron temperature.

Figure 11 shows Poincaré plots of the magnetic field at four times in the 3D calculation presented in Fig. 8. At time  $t = 3000 \tau_A$ , the surfaces first distort as the unstable modes start to grow. By time  $t = 3500 \tau_A$ , the surfaces have broken up in the center. They remain broken until the end of the calculation, at  $t = 6000 \tau_A$ , although the outer surfaces are intact.

The midplane temperature profiles for the 2D and 3D calculations at the initial and three additional times are shown in Fig. 12. Comparing the 2D and 3D profiles from Fig. 12, we see that the first two time slices are essentially identical. However, at some time between  $t = 2000 \tau_A$  and  $t = 4000 \tau_A$ , the primary effect of the heating was to broaden the 3D calculation temperature profile, not uniformly increase it as in the 2D calculation. This broadening of the temperature profile as  $\beta$  increases is qualitatively similar to the NSTX experimental result presented in Ref. 10 and shown in Fig. 6(a).

Because the  $\beta$  vs time plots for the 2D and 3D calculations were the same, we can plot the maximum temperature as a function of  $\beta$  for the 2D and 3D calculations. This is done in Fig. 13, making clear that a critical  $\beta$  exists at which time surface breakup occurs and the central electron temperature no longer monotonically increases with  $\beta$  in 3D.

## VI. MORE ON NSTX SHOT 124 379

Figure 14 gives a time history of some of the parameters calculated from equilibrium reconstructions of NSTX shot 124 379 and their MHD stability properties for toroidal modes 1–9 as calculated

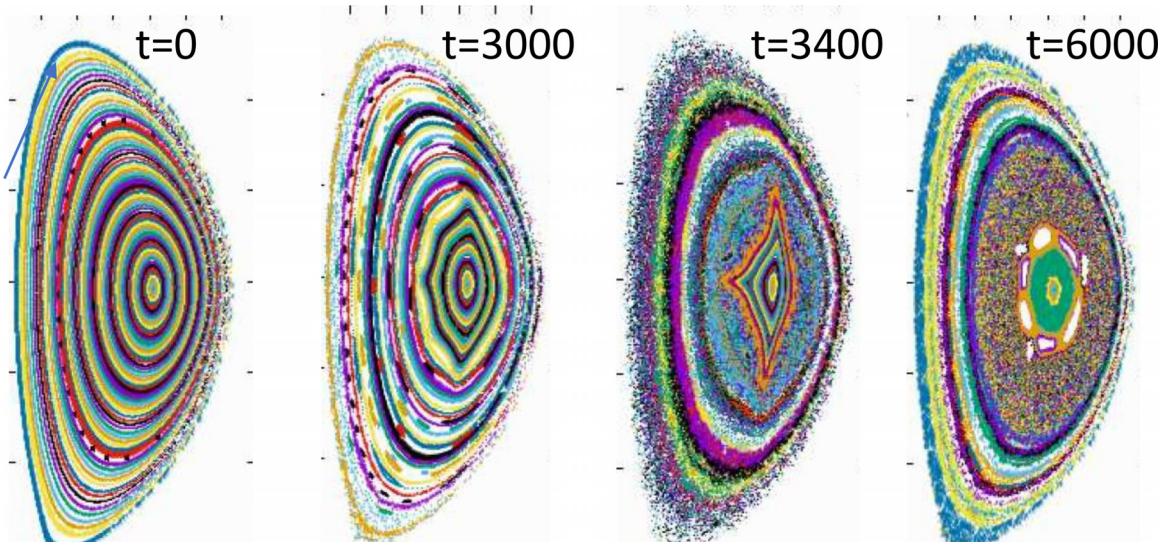


FIG. 11. Poincaré plots of the magnetic field at four times during the calculation of Fig. 8.

every 10 ms from 500 to 700 ms. There is obviously a lot of scatter in these results, and we do not have meaningful error bars, but we think that the overall trends are relevant.

All MHD modes are stable before  $t = 550$  ms. From  $t = 500$  ms to about  $t = 650$  ms, there is a general trend for the  $\beta$  to be increasing and for the central safety factor,  $q_0$  to be decreasing. At about  $t = 560$  ms, calculations show the toroidal mode numbers  $n = 3, 5, 7,$  and  $8$  suddenly become unstable. Although the poloidal mode number is generally not a good quantum number in a torus, we see from Fig. 2 and from our other calculations that the poloidal mode

number can be easily identified for these modes, which are  $(4,3), (7,5), (10,7),$  and  $(11,8)$ . At this time,  $q_0 \approx 1.3$ , so that each of these  $(m,n)$  modes has a  $m-nq$  resonance where the mode locates, very near the center.

This largely remains the case for the next 100 ms. Although the exact modes that are unstable change during this time, the majority of the unstable modes are such that they have a resonance very near the center, at values of  $m/n$  varying from 1.2 to 1.44. The non-resonant  $(1,1)$  mode is the exception, as are a few (barely) non-resonant  $(5,4)$  modes. We, thus, expect mode activity, surface breakup, and

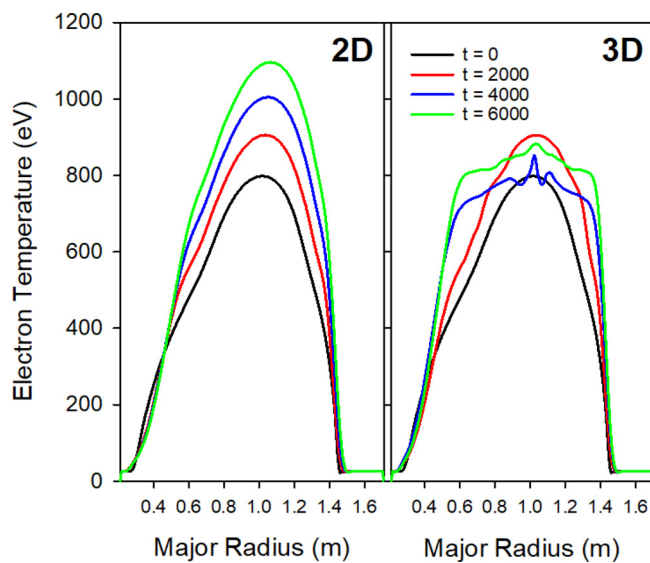


FIG. 12. Midplane electron temperature at the initial and three additional times for the 3D calculation (right) and for a 2D calculation (left) with the same transport coefficients and heat source (left).

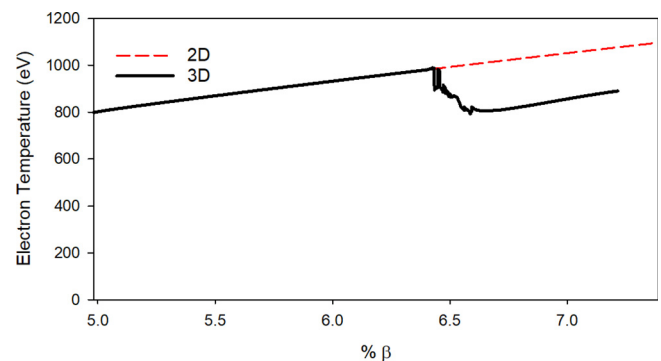
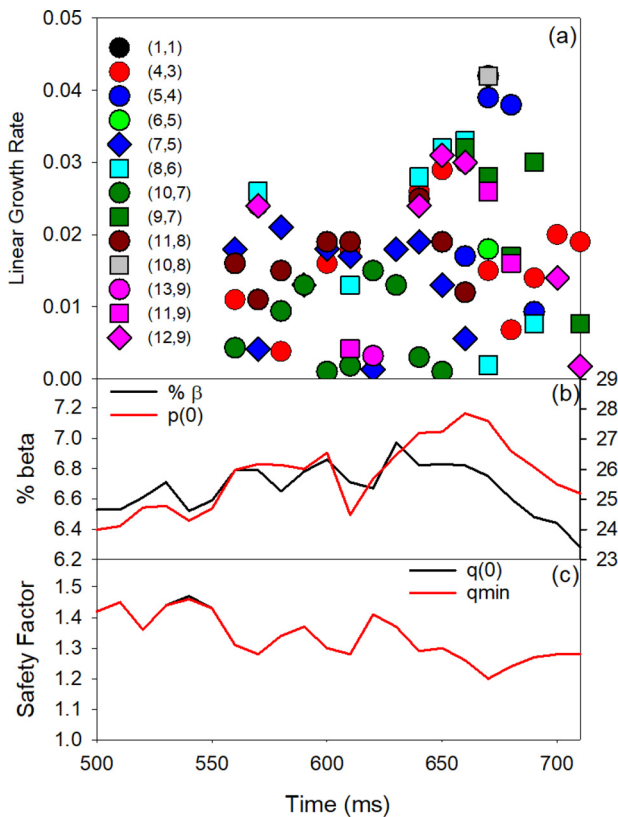


FIG. 13. Graph of the central temperature vs  $\beta$  for the sequence shown in Fig. 8. In the 2D calculation, the temperature increases linearly with  $\beta$ . In the 3D calculation, the temperature sharply decreases at about  $\beta = 6.4\%$ .

TABLE II. Poloidal mode number  $m$  for each of first seven unstable modes shown in Fig. 9.

$n$	2	4	6	8	10	11	13
$m$	3	6	9	12	15	16	19



**FIG. 14.** (a) Linear growth rates for unstable modes with toroidal mode numbers 1–9 calculated every 10 ms. (b) Percent  $\beta$  and central pressure in kilobar from equilibrium reconstructions. (c) Central and minimum safety factor from equilibrium reconstructions.

temperature flattening during this entire time, which is consistent with what was observed for this discharge.

**VII. SUMMARY AND DISCUSSION**

In summary, we have demonstrated a new mechanism that could limit the central temperature and peakedness of the pressure profile in a ST. There are indications that this also occurs in MAST.<sup>36</sup> The details and significance of this mechanism clearly depend on the form of the pressure and current profiles and need to be further explored for a range of discharges. However, it is clear that the possible destruction of surfaces by ideal MHD instabilities should be taken into account when performing data analysis and when projecting ST parameters for future devices.

The unstable modes that we have identified have values of  $m/n$  ranging from 1.2 to 1.5 in equilibria with  $q_0$  in the same range, or slightly lower, and with low central shear. It may be that this is a “danger zone,” which, if avoided, would lead to better confinement. This conclusion is the result of numerical exploration and remains to be definitively determined by analytical work and experimental data.

We have gained some insight as to why the linear growth rates of the modes shown in Figs. 1 and 9 are oscillatory functions of the toroidal mode number  $n$ . Figures 3 and 10 illustrate that for these profiles,

there is a narrow range of  $q$  that exists in a sufficiently low shear region, above  $q_0$ , and there must be a poloidal mode number  $m$  that puts  $m/n$  in that narrow low shear region. The existence of such a  $m$  is certainly different for different  $n$ , particularly for odd and even values.

We note here that there are also reports of confinement degradation in high- $\beta$  operation of conventional aspect ratio tokamaks as well when infernal modes are observed. This has likely occurred in JET,<sup>37,38</sup> TFTR,<sup>39</sup> JT60-U,<sup>40</sup> DIII-D,<sup>41</sup> and JT60-SA.<sup>42</sup> Model  $R/a = 4$  equilibria that exhibit infernal modes are discussed in Ref. 3 and further in the Appendix. Future studies will help clarify what role the aspect ratio and plasma shaping plays in this mechanism and how best to minimize its effects.

These studies use a fixed ratio of parallel to isotropic thermal conductivity of  $\kappa_{||}/\kappa = 10^7$ , which was somewhat artificial and arbitrary. We have found that the final results depend only weakly on this ratio since for sufficiently high values, the process is self-regulating as the large parallel transport reduces the local pressure gradient and thus removes the drive, returning the configuration to a stable state. Anticipated future work will include kinetic extensions of the MHD model to better understand the relative effect of these instabilities on the ions and electrons and if wave-particle resonances are important.

It is also worth noting that the M3D-C1 code has a “reduced MHD” option that advances only the poloidal flux, the vorticity, and the pressure.<sup>17</sup> The infernal modes shown in Figs. 1 and 2 were not found with that option, and so future analysis studies should use the full MHD model as was done here.

**ACKNOWLEDGMENTS**

We are grateful to Alan Turnbull of General Atomics for using the GATO ideal MHD code to verify the existence of an unstable (4,3) mode in the NSTX 124379 equilibrium we examined in Sec. III with a very similar mode structure to what was presented here. This work was supported by the U.S. DoE Award No. DE-AC02-09CH11466, and the SciDAC Center for Tokamak Transient Simulations (CTTS). The authors acknowledge essential software support from J. Chen and the SCOREC team at RPI.

**AUTHOR DECLARATIONS**

**Conflict of Interest**

The authors have no conflicts to disclose.

**Author Contributions**

**Stephen C. Jardin:** Conceptualization (lead); Funding acquisition (equal); Investigation (lead); Methodology (lead); Software (equal); Validation (equal); Writing – original draft (lead). **Nathaniel Ferraro:** Conceptualization (supporting); Funding acquisition (supporting); Software (equal); Writing – review & editing (supporting). **Walter Guttenfelder:** Conceptualization (supporting); Funding acquisition (supporting); Writing – original draft (equal). **Stanley M. Kaye:** Conceptualization (supporting); Data curation (supporting); Funding acquisition (equal); Investigation (supporting); Writing – original draft (supporting). **Stefano Munaretto:** Conceptualization (supporting); Data curation (lead); Investigation (supporting); Validation (equal); Writing – review & editing (equal).

DATA AVAILABILITY

The data that support the findings of this study are available from the corresponding author upon reasonable request.

APPENDIX: STABILITY OF MODEL EQUILIBRIUM

Here, we describe a parameter scan of the stability of a class of circular, aspect ratio  $R/a = 4.0$  equilibrium that extends the study published in Ref. 3. The pressure and safety factor profiles are given by

$$q(\psi) = q_0 + q_1\psi^{\alpha_1}, \tag{A1}$$

$$p(\psi) = p_0(1 - \psi^{\alpha_2})^{\alpha_1}. \tag{A2}$$

Following Ref. 3, we set the profile factors to  $\alpha_q = 4.0$ ,  $\alpha_1 = 4.0$ ,  $\alpha_2 = 1.5$ . Although Ref. 3 considered only  $q_0 = 1.05$ , we varied  $q_0$  from 1.05 to 2.05 in steps of 0.1 and set  $q_1 = 3.10 - q_0$ , thus fixing the value at the limiter to 3.10.

In Fig. 15, we plot the unstable mode growth rates as a function of toroidal mode number for a family of equilibrium, all with  $\beta = 1.2\%$  (normalized  $\beta_N = 2.6$ ). These low- $n$  modes are seen to be unstable if there exists an integer  $m$  such that the ratio  $m/n$  is very close to  $q_0$ . The unstable modes can be both resonant, with  $m/n \geq q_0$ , and non-resonant,<sup>43</sup> with  $m/n \leq q_0$ . Equilibrium in this series with  $1.55 < q_0 < 2.05$  was all found to be stable for this  $\beta$  value and these toroidal mode numbers. Lowering the  $\beta$  to 1% left only the  $n=1$  unstable for  $q_0 = 1.05$ , the  $n=6$  unstable for  $q_0 = 1.15$ , and the  $n=2$  unstable for  $q_0 = 1.45$ . Lowering  $\beta$  further to 0.8% resulted in all modes being stable for all  $q_0$ .

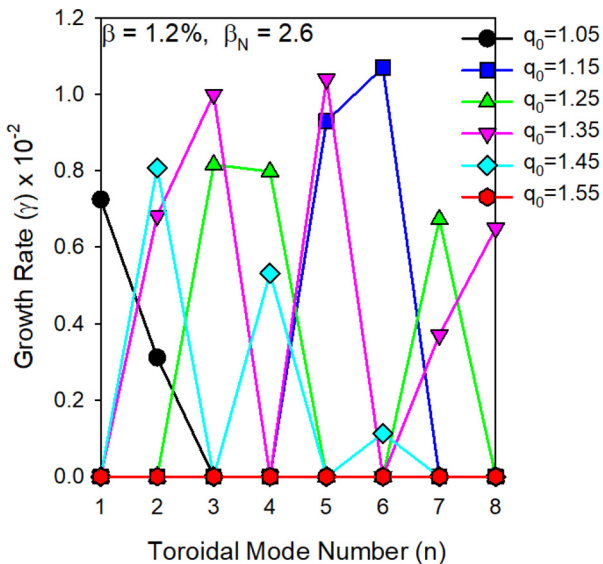


FIG. 15. Unstable mode growth rate as a function of toroidal mode number  $n$  for a series of six circular  $R/a = 4$  equilibria with central safety factor  $q_0$  ranging from 1.05 to 1.55, with the profiles defined by Eqs. (A1) and (A2). The central pressure,  $p_0$  in Eq. (A2), was adjusted to give volume averaged  $\beta = 1.2\%$ , which corresponds to a normalized  $\beta_N = 2.6$ .

REFERENCES

- <sup>1</sup>S. C. Jardin, N. M. Ferraro, W. Guttenfelder, S. M. Kaye, and S. Munaretto, *Phys. Rev. Lett.* **128**, 245001 (2022).
- <sup>2</sup>M. Ono, S. M. Kaye, Y.-K. M. Peng, G. Barnes, W. Blanchard, M. D. Carter, J. Chrzanowski, L. Dudek, R. Ewig, D. Gates *et al.*, *Nucl. Fusion* **40**, 557 (2000).
- <sup>3</sup>J. Manickam, N. Pomphrey, and A. Todd, *Nucl. Fusion* **27**, 1461 (1987).
- <sup>4</sup>S. M. Kaye, R. E. Bell, D. Gates, B. P. LeBlanc, F. M. Levinton, J. E. Menard, D. Mueller, G. Rewoldt, S. A. Sabbagh, W. Wang, and H. Yuh, *Phys. Rev. Lett.* **98**, 175002 (2007).
- <sup>5</sup>S. M. Kaye, F. M. Levinton, D. Stutman, K. Tritz, H. Yuh, M. G. Bell, R. E. Bell, C. W. Domier, D. Gates, W. Horton *et al.*, *Nucl. Fusion* **47**, 499–509 (2007).
- <sup>6</sup>M. Valovic, R. Akers, G. Cunningham, L. Garzotti, R. Lloyd, D. Muir, A. Patel, D. Taylor, M. Turnyanskiy, and M. Walsh, *Nucl. Fusion* **49**, 075016 (2009).
- <sup>7</sup>G. S. Kurskiv, N. N. Bakharev, V. V. Bulanin, F. V. Chernyshev, V. K. Gusev, N. A. Khromov, E. O. Kiselev, V. B. Minaev, I. V. Miroshnikov, E. E. Mukhin *et al.*, *Nucl. Fusion* **59**, 066032 (2019).
- <sup>8</sup>G. S. Kurskiv, V. K. Gusev, N. V. Sakharov, I. M. Baiachenkov, E. O. Kiselev, N. A. Khromov, V. B. Minaev, I. V. Miroshnikov, M. I. Patrov, A. V. Petrov *et al.*, *Nucl. Fusion* **61**, 064001 (2021).
- <sup>9</sup>S. M. Kaye, S. Gerhardt, W. Guttenfelder, R. Maingi, R. E. Bell, A. Diallo, B. P. LeBlanc, and M. Podesta, *Nucl. Fusion* **53**, 063005 (2013).
- <sup>10</sup>D. Stutman, L. Delgado-Aparicio, N. Gorelenkov, M. Finkenthal, E. Fredrickson, S. Kaye, E. Mazzucato, and K. Tritz, *Phys. Rev. Lett.* **102**, 115002 (2009).
- <sup>11</sup>N. Gorelenkov, D. Stutman, R. Tritz, A. Boozer, L. Delgado-Aparicio, E. Fredrickson, S. Kaye, and R. White, *Nucl. Fusion* **50**, 084012 (2010).
- <sup>12</sup>N. Crocker, W. A. Peebles, S. Kubota, J. Zhang, R. E. Bell, E. D. Fredrickson, N. N. Gorelenkov, B. P. LeBlanc, J. E. Menard, M. Podesta *et al.*, *Plasma Phys. Controlled Fusion* **53**, 105001 (2011).
- <sup>13</sup>N. Crocker, E. D. Fredrickson, N. N. Gorelenkov, W. A. Peebles, S. Kubota, R. E. Bell, A. Diallo, B. P. LeBlanc, J. E. Menard, M. Podesta, K. Tritz, and H. Yuh, *Nucl. Fusion* **53**, 043017 (2013).
- <sup>14</sup>E. V. Belova, N. N. Gorelenkov, N. A. Crocker, J. B. Lestz, E. D. Fredrickson, S. Tang, and K. Tritz, *Phys. Plasmas* **24**, 042505 (2017).
- <sup>15</sup>N. A. Crocker, S. Kubota, W. A. Peebles, T. L. Rhodes, E. D. Fredrickson, E. Belova, A. Diallo, B. P. LeBlanc, and S. A. Sabbagh, *Nucl. Fusion* **58**, 016051 (2018).
- <sup>16</sup>A. H. Boozer, “The rapid destruction of toroidal magnetic surfaces,” *Phys. Plasmas* **29**, 022301 (2022).
- <sup>17</sup>S. C. Jardin, N. Ferraro, J. Breslau, and J. Chen, *Comput. Sci. Discovery* **5**, 014002 (2012).
- <sup>18</sup>I. B. Bernstein, E. A. Frieman, M. D. Kruskal, and R. M. Kulsrud, *Proc. R. Soc. London, Ser. A* **244**, 17–49 (1958).
- <sup>19</sup>H. P. Furth, J. Killeen, M. N. Rosenbluth, and B. Coppi, *CULHAM IAEA Conference* (IAEA, 1965), Vol. I, pp. 103–126.
- <sup>20</sup>J. M. Greene and J. L. Johnson, *Plasma Phys.* **10**, 729–745 (1968).
- <sup>21</sup>C. Mercier, *Nucl. Fusion* **1**, 47 (1960).
- <sup>22</sup>D. Dobrott, D. B. Nelson, J. M. Greene, A. H. Glasser, M. S. Chance, and E. A. Frieman, *Phys. Rev. Lett.* **39**, 943 (1977).
- <sup>23</sup>J. W. Connor, R. J. Hastie, and J. B. Taylor, *Proc. R. Soc. London, Ser. A* **365**, 1–17 (1979).
- <sup>24</sup>R. C. Grimm, J. M. Greene, and J. L. Johnson, in *Controlled Fusion*, Methods in Computational Physics: Advances in Research and Applications, Volume 16 (Academic Press, 1976), pp. 253–280.
- <sup>25</sup>L. C. Bernard, F. J. Helton, and R. W. Moore, *Comput. Phys. Commun.* **24**, 377 (1981).
- <sup>26</sup>J. P. Freidberg, *Ideal Magneto-Hydro-Dynamics* (Plenum Press, New York, 1987).
- <sup>27</sup>J. A. Breslau, M. S. Chance, J. Chen, G. Y. Fu, S. Gerhardt, N. Gorelenkov, S. C. Jardin, and J. Manickam, *Nucl. Fusion* **51**, 063027 (2011).
- <sup>28</sup>L. Zakharov, *Nucl. Fusion* **18**, 335 (1978).
- <sup>29</sup>R. Dewar, J. Manickam, R. Grimm, and M. Chance, *Nucl. Fusion* **21**, 493 (1981).
- <sup>30</sup>L. A. Charlton, B. A. Carreras, and V. E. Lynch, *Phys. Fluids B* **2**, 1574 (1990).
- <sup>31</sup>J. D. Huba, *NRL Plasma Formulary* (Naval Research Laboratory, 2013).
- <sup>32</sup>L. D. Landau and E. M. Lifschitz, *Fluid Mechanics*, 1st ed. (Pergamon Press, 1959), Vol. 6.
- <sup>33</sup>S. C. Jardin, *J. Comput. Phys.* **200**, 133–152 (2004).
- <sup>34</sup>G. Bateman and M. Peng, *Phys. Rev. Lett.* **38**, 829 (1977).

- <sup>35</sup> $\beta_N = 2.9$ : NSTX shot 120 451@400 ms,  $\beta_N = 3.6$ : NSTX shot 120 434@400 ms,  $\beta_N = 4.3$ : NSTX shot 120 446@400 ms.
- <sup>36</sup>I. T. Chapman, W. A. Cooper, J. P. Graves, M. P. Gryaznevich, R. J. Hastie, T. C. Hender, D. F. Howell, M. D. Hua, G. T. Huysmans, D. I. Keeling *et al.*, *Nucl. Fusion* **51**, 073040 (2011).
- <sup>37</sup>O. J. Kwon, I. T. Chapman, P. Buratti, H. Han, Y. Na, and JET-EFDA Contributors, *Plasma Phys. Controlled Fusion* **54**, 045010 (2012).
- <sup>38</sup>L. A. Charlton, L. R. Baylor, A. W. Edwards, G. W. Hammett, W. A. Houlberg, P. Kupschus, V. E. Lynch, S. L. Milora, J. O'Rourke, and G. L. Schmidt, *Nucl. Fusion* **31**, 1835 (1991).
- <sup>39</sup>Z. Chang, E. D. Fredrickson, J. D. Callen, K. M. McGuire, M. G. Bell, R. V. Budny, C. E. Bush, D. S. Darrow, A. C. Janos, L. C. Johnson *et al.*, *Nucl. Fusion* **34**, 1309 (1994).
- <sup>40</sup>T. Ozeki, M. Azumi, Y. Kamada, S. Ishida, Y. Neyatani, and S. Tokuda, *Nucl. Fusion* **35**, 861 (1995).
- <sup>41</sup>A. D. Turnbull, D. P. Brennan, M. S. Chu, L. L. Lao, and P. B. Snyder, *Fusion Sci. Technol.* **48**, 875–905 (2005).
- <sup>42</sup>A. Bierwage, M. Toma, and K. Shinohara, *Plasma Phys. Controlled Fusion* **59**, 125008 (2017).
- <sup>43</sup>A. Wright and N. Ferraro, *Phys. Plasmas* **28**, 072511 (2021).